Journal of Building Engineering 75 (2023) 106988

Contents lists available at ScienceDirect

Journal of Building Engineering

journal homepage: www.elsevier.com/locate/jobe

Mechanical properties, microstructural characteristics and heat treatment effects of WAAM stainless-steel plate material

Yang Zhao [a, c], Yin Chen [a], Zhen Wang [b, *], Jun Ye [d, **], Weijian Zhao [a]

[a] College of Civil Engineering and Architecture, Zhejiang University, Hangzhou, 310058, China
[b] Department of Civil Engineering, Hangzhou City University, Hangzhou, 310015, China
[c] School of Civil Engineering, Shaoxing University, Shaoxing, 312000, China
[d] School of Civil Engineering, University of Leeds, Leeds, LS2 9JT, UK

ARTICLE INFO

Keywords:
Metal 3D printing
Structural tests
Mechanical properties
Microstructure
Printing paths
Heat treatment

ABSTRACT

Wire and arc additive manufacturing (WAAM) is a technology that enables the in-situ manufacturing of large-scale components efficiently for the construction industry. However, uncertainties persist regarding the characteristics of WAAM materials, such as anisotropic mechanical properties and their correlation with metallographic structure and fracture morphology, printing paths, and heat treatment. More experimental data is also required to establish design methods for the application of WAAM stainless steel in construction. To bridge these knowledge gaps, a comprehensive series of tensile tests was therefore conducted on WAAM stainless steel. Four deposition plates were fabricated using WAAM technique with different printing paths, and tensile coupons were extracted in three directions from each plate. Tensile tests were conducted to evaluate the mechanical properties of the material. Optical microscopy (OM) and scanning electron microscopy (SEM) were then employed to examine the metallographic structure of the material and the fracture morphology of the coupons. The results showed that the WAAM material had good yield and ultimate strengths but slightly lower ductility than conventional stainless steel. Anisotropy was observed in some but not all printing paths, and Young's modulus, ultimate strain and fracture strain exhibited the highest values in the 45° specimens. The grain size of the plate was influenced by its printing path. Mechanical properties were associated with the metallographic structure and fracture morphology. Compared to the heat-treated counterpart, the non-heat-treated material exhibited higher yield and ultimate strengths but lower ductility.

1. Introduction

Additive manufacturing (AM), also known as 3D printing and rapid prototyping is a process of joining materials to make parts from 3D model data, usually layer upon layer, as opposed to subtractive manufacturing [1]. AM offers the benefits of high digitalization and geometric freedom, reduced material consumption and waste, and easy customisation, resulting in its increasingly widespread application across multiple industries. AM is considered a critical component of Industry 4.0 [2–5].

According to ISO/ASTM 52900:2021 [1], AM techniques can be classified into seven categories: powder bed fusion (PBF), directed energy deposition (DED), material extrusion (MEX), material jetting (MJT), binder jetting, (BJT), sheet lamination (SHL) and vat photopolymerization (VPP). Currently, AM processes of metallic materials generally include PBF, DED, BJT and SHL [6]. Wire and

* Corresponding author.
** Corresponding author.
E-mail addresses: wangzhen@hzcu.edu.cn (Z. Wang), j.ye2@leeds.ac.uk (J. Ye).

https://doi.org/10.1016/j.jobe.2023.106988
Received 10 April 2023; Received in revised form 24 May 2023; Accepted 31 May 2023
Available online 2 June 2023

arc additive manufacturing (WAAM) is a DED technique that employs welding arcs as the heat source and wire as the raw material to build components layer by layer [7]. The welding processes for WAAM include gas tungsten arc welding (GTAW), gas metal arc welding (GMAW), and plasma arc welding (PAW) [2]. Cold metal transfer (CMT) used in this study is a GMAW-based technology that improves the welding process through controlled metal deposition and low heat input. CMT has a broad range of applications, such as AM, cladding, composite joint pin fabrication, and crack repair welding [8]. Various raw materials are used for AM, including metal, ceramic, polymer and composite [1]. Austenitic stainless steel is a widely used metal for the construction industry due to its good corrosion resistance and relatively low cost [9], which contributes to the construction of the world's first stainless-steel metal bridge [10].

Among various AM processes, WAAM is well-suited for the production of medium to large-scale components due to its high deposition rates, relatively low costs, and unlimited build volume [7]. Furthermore, it enables automated on-site production of building parts [2]. Novel connectors and truss structures, typically optimized with topology optimization methods for enhanced material efficiency, have been realized using WAAM, such as an innovative stainless steel connector for spatial shells designed collaboratively by MX3D and Takenaka (Fig. 1(a)) [11] and an optimized truss structure by Ye et al. (Fig. 1(b)) [12]. For large-scale WAAM structural systems, two footbridges have been manufactured in Amsterdam (Fig. 1(c)) [10] and Darmstadt (Fig. 1(d)) [13], with the latter constructed in situ. Overall, WAAM has the potential to drive significant advancements in the construction industry.

The behaviour of structural components or a structural system is heavily dependent on the constitutive relationships of the related building materials. Thus, investigating the properties of WAAM material is crucial for the wider application of WAAM technology in the construction industry. Recent studies have increasingly focused on the material properties of stainless steel produced using WAAM. Tensile tests were conducted on WAAM stainless steel using raw materials such as 304L [14–16], 316L [17–19], and 308LSi [20–25] to evaluate the mechanical properties. The primary printing strategy employed was layer-by-layer [15–25], whereas the dot-by-dot approach was also used in a few cases [14,25]. These studies revealed that: 1) the tensile strength and ductility of WAAM stainless steel are comparable to those of conventionally fabricated counterparts; 2) the material responses exhibit significant anisotropy; 3) the geometric irregularity inherent to the WAAM process effectively decreases some mechanical properties; 4) tensile specimens with varying thicknesses exhibit differences in mechanical properties; 5) inspection of the fracture surfaces reveals ductile fracture behaviour in tensile specimens. Based on data obtained from tensile tests, constitutive models have been initially established to describe the anisotropic material response of WAAM stainless steel in the elastic [20,23] and plastic range [20], and design values for key mechanical parameters have been proposed [26]. Microstructure studies have used electron backscatter diffraction (EBSD), optical microscope (OM) and scanning electron microscope (SEM) to examine the crystallographic texture and the metallographic structure [14,16,21,24,27], and results revealed that the anisotropy in WAAM material behaviour results from a strong crystallographic texture. However, study into the fracture surface morphology of WAAM material and its correlation to mechanical properties is deficient. The effects of printing paths, such as parallel and oscillation strategies, on WAAM-fabricated mild steel [28,29], high strength

(a) Takenaka connector [11]

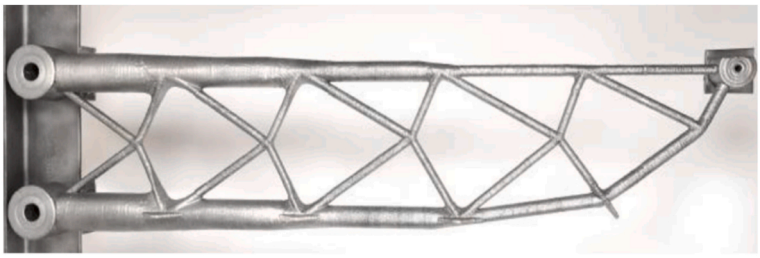

(b) optimized truss structure [12]

(c) the footbridge in Amsterdam [10]

(d) the footbridge in Darmstadt [13]

Fig. 1. WAAM structural components in the construction field.

steel [30], and martensitic stainless steel [31,32] have been investigated. However, the effect on WAAM austenitic stainless steel remains unexplored. Heat treatment also affects the mechanical properties and microstructures of WAAM austenitic stainless steel [27,33,34], but data on this topic are scarce.

WAAM material properties are significantly influenced by various process inputs, including manufacturing equipment, printing method, printing path, processing parameter and heat treatment method. Even with a fixed set of process inputs, material properties may vary considerably [14,35,36]. Therefore, further experimental research is necessary to establish design guidance and specification for the application of WAAM stainless steel in construction. In particular, the microscopic causes of mechanical properties, the effect of different printing paths, and the effect of heat treatment on WAAM austenitic stainless steel should be studied due to the scarcity of available data. This study conducts a series of experiments including tensile tests, metallographic observation, and SEM fracture surface observation to investigate the mechanical properties, the correlation between mechanical properties and microstructures, and the effects of heat treatments and different printing paths. Four deposition plates were fabricated using CMT-WAAM (cold metal transfer wire and arc additive manufacturing) with four distinct printing paths. From each plate, nine tensile coupons were extracted using wire cutting in three different directions (0°, 45°, and 90°to the long side of the deposition plate). Tensile tests were performed to study the mechanical properties and degree of anisotropy. OM and SEM were utilized to examine the metallographic structure of the material and the fracture surfaces of specimens after tensile tests, and the relationship between the microstructural characteristics and mechanical properties was analysed. It should be noted that the author's research group previously conducted a series of tensile tests on specimens fabricated with an identical procedure as this paper, except that the specimens were subjected to solution heat treatment. Thus, the mechanical properties obtained from this paper were compared to those of the previous study to investigate the effect of solution heat treatment on mechanical properties.

2. Preparation of test specimens

A series of smooth specimens with nominal thicknesses of 4 mm and 8 mm were to be prepared for the tensile tests. Given the undulating surface of WAAM material, three deposition plates with nominal dimensions of 270 mm × 230 mm × 6 mm and one deposition plate with nominal dimensions of 300 mm × 260 mm × 10 mm were fabricated using CMT-WAAM technology (Fig. 2). The process parameters are provided in Table 1. A commercial 316L stainless steel plate with dimensions of 400 mm × 400 mm × 60 mm was used as the substrate, and was polished and cleaned before the deposition process. The raw material used was a 1.2 mm diameter 316L stainless steel wire, with its chemical composition shown in Table 2.

(a) CMT-WAAM equipment (b) Manufacturing process

Fig. 2. WAAM production equipment and process.

Table 1
Process parameters of WAAM deposition.

Process parameter	Form/range of value
power form	CMT
working current	110–175 A
working voltage	18–22 V
scanning speed	400–600 mm/min
wire feed rate	5.5–7.2 m/min
deposition efficiency	0.8–1.6 kg/h
layer height	2.0–3.5 mm
ambient temperature	15–25 °C
interlayer temperature	80–130 °C
wire material	316 L
wire diameter	1.2 mm
protection gas	97%Ar + 3%CO_2
gas flow rate	20–30 L/min

Table 2
Chemical composition of 316L stainless steel wire.

Composition	C	Mn	Si	P	S	Cu	Ni	Cr	Mo
316L steel	≤ 0.03	1.0–2.5	0.3–0.65	≤ 0.03	≤ 0.03	≤ 0.75	11.0–14.0	18.0–20.0	2.0–3.0

The deposition plates were fabricated by moving the welding torch back and forth along the Y direction, as illustrated in Fig. 3. Fig. 4 shows the path of the welding torch's movement for each plate. The deposition plates were labelled as *AB*-T*C*, where *A*, *B*, and *C* denote variables. The letter '*A*' indicated the plate orientation: V for vertical and H for horizontal to the level surface. The letter '*B*' indicated printing layer direction: L for along the long side and S for along the short side of plates. The letter '*C*' represented the thicknesses of tensile specimens extracted from the plate. Note that for convenience of subsequent expression, the nominal thicknesses of

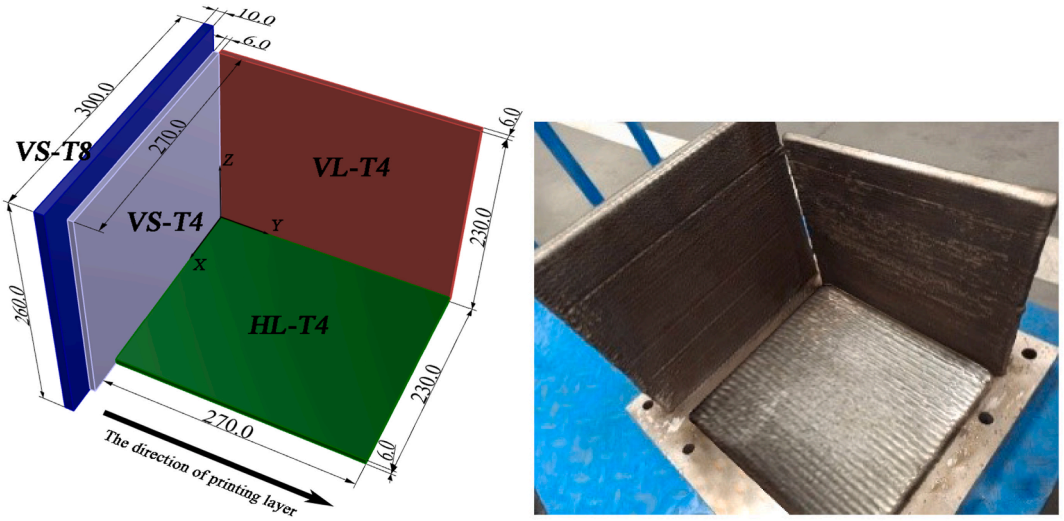

(a) Digital model (b) Real object

Fig. 3. Deposition plates.

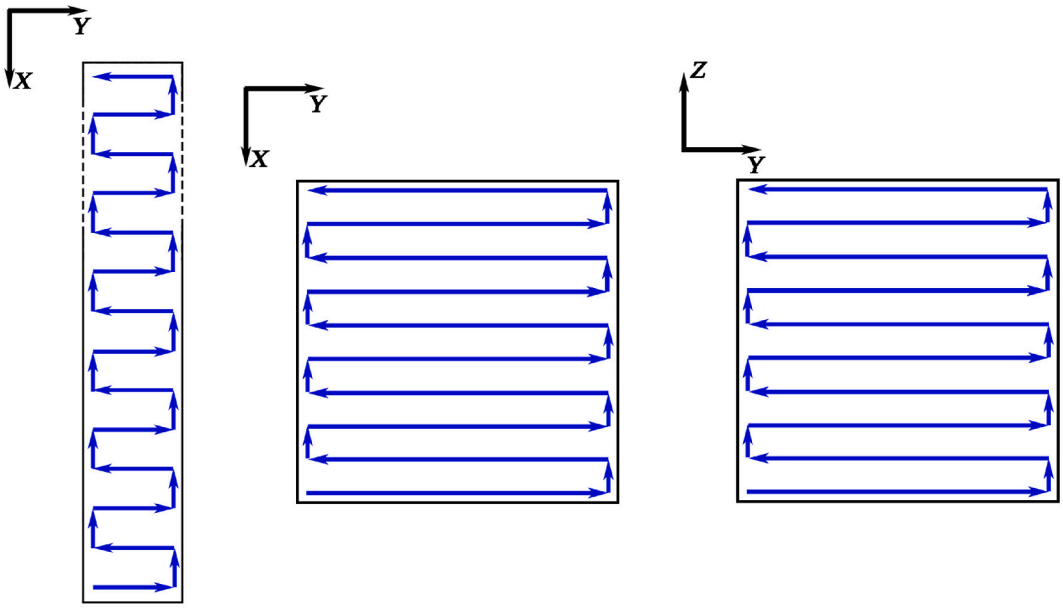

(a) Plates VS-T4 and VS-T8 (b) Plate HL-T4 (c) Plate VL-T4

Fig. 4. The path of the torch's movement.

smooth tensile specimens (4 mm and 8 mm) extracted from plates were used instead of the thicknesses of the as-built WAAM plates (6 mm and 10 mm). For example, Plate VL-T4 was a vertical plate with its printing layer along the long side of the plate, from which tensile specimens with a nominal thickness of 4 mm were extracted.

As shown in Fig. 5(a) and (b), nine tensile specimens were extracted from each deposition plate in three distinct directions (0°, 45°, and 90°to the longer side of the plates). Surface undulations were removed using wire cutting to produce smooth specimens with nominal thicknesses of 4 mm and 8 mm (Fig. 5(c)), as the effect of geometric irregularity was outside the scope of this study. The dimensions of the tensile specimens, which conform to the GB/T 228.1–2010 standard [37], are shown in Fig. 6.

The tensile specimens were labelled using the following format: 'plate label - extraction angle to the longer side of the plate - the serial number within the same class'. For example, Coupon VL-T4-45-1 represents specimen number 1 of the three specimens extracted at a 45° angle to the longer side of plate VL-T4. For convenience, the three coupons within the same class are denoted as one group. For instance, Group VL-T4-45 refers to Coupons VL-T4-45-1~VL-T4-45-3.

3. Test scheme and data processing

This section presents tests conducted on WAAM specimens, including geometric measurements, tensile tests, metallographic scanning test, and fracture surface SEM test. The data processing approaches are also demonstrated.

3.1. Geometric measurement and post-processing

A non-contact geometric measurement method, 3D scanning, was used to obtain the geometric model and cross-sectional area of each specimen, as shown in Fig. 7(a). To examine the dimensional variations across different cross-sections, four typical specimens (HL-T4-45-2, VL-T4-0-1, VS-T4-0-1, and VS-T8-90-3) were analysed. The specimens were contoured at 0.2 mm intervals along the parallel tensile segment, as illustrated in Fig. 7(b), and the area and thickness of each contour were measured. The results showed that the relative differences between the maximum and minimum values of both area and thickness were less than 0.01 for all four specimens, as shown in Table 3. In Table 3, A_{max}, A_{min}, t_{max} and t_{min} denote the maximum area, minimum area, maximum thickness and minimum thickness along the parallel tensile segment of each specimen, respectively. Thus, the parallel tensile segments of the specimens were considered to have an equal cross-section. This demonstrated that the wire-cutting process was accurate enough to eliminate geometric irregularity. Table 4 presents the cross-sectional areas and thicknesses of all specimens, which were determined as the average of the corresponding values along the parallel tensile segment.

3.2. Tensile test and data processing methods

Tensile tests were conducted on an INSTRON 8802 machine with a loading capacity of 250 kN in accordance with GB/T228.1–2010 [37]. The controlled displacement method was used for loading at a crosshead speed of 1 mm/min. Three methods

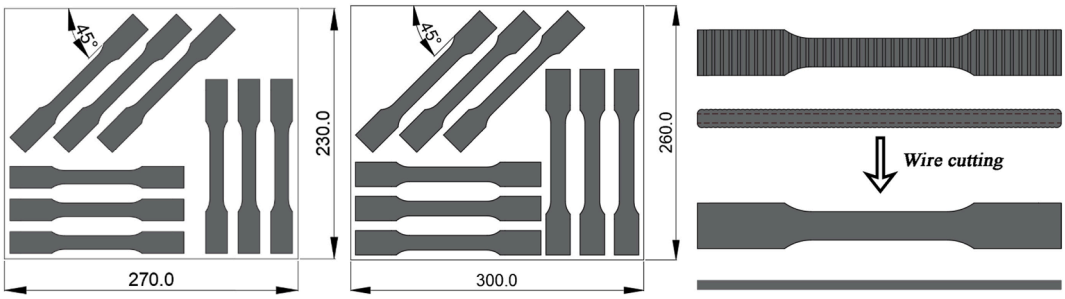

(a) Plates HL-T4, VL-T4, VS-T4 (b) Plate VS-T8 (c) Wire cutting processing

Fig. 5. Sampling scheme of tensile coupons from WAAM plate.

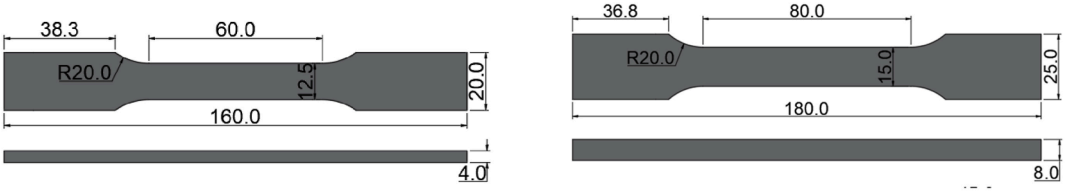

(a) Specimen from plates HL-T4, VL-T4, VS-T4 (b) Specimen from plate VS-T8

Fig. 6. Dimensions of the tensile specimens.

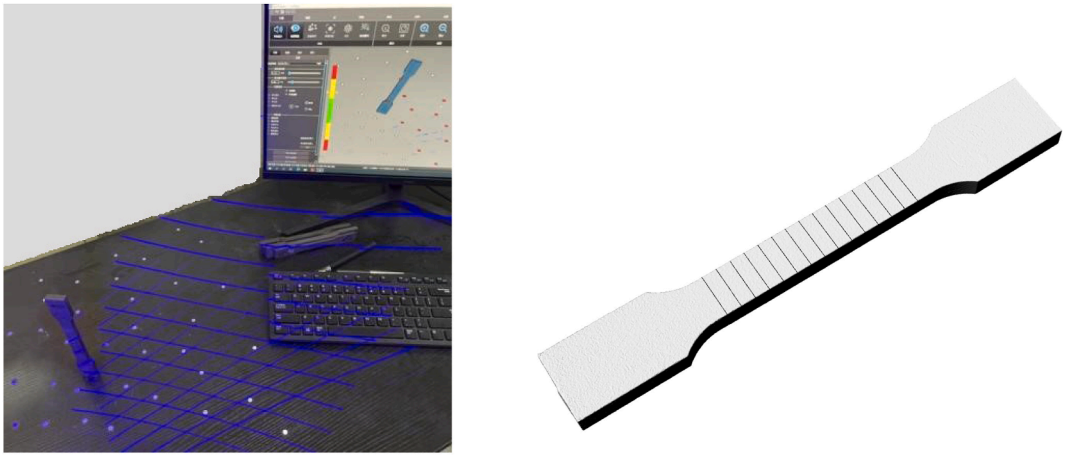

(a) Scanning process (b) Geometric model

Fig. 7. Scanning process and geometric model of the tensile coupon obtained from the scanning data.

Table 3
Dimensional variations across different cross-sections of four typical specimens.

Coupon	A_{max} (mm^2)	A_{min} (mm^2)	$(A_{max}$-$A_{min})/A_{min}$	t_{max} (mm)	t_{min} (mm)	$(t_{max}$-$t_{min})/t_{min}$
HL-T4-45-2	49.84	49.57	0.0054	4.01	3.98	0.0075
VL-T4-0-1	48.10	47.81	0.0061	3.90	3.87	0.0078
VS-T4-0-1	48.94	48.64	0.0062	3.96	3.93	0.0076
VS-T8-90-3	123.01	122.16	0.0070	8.24	8.17	0.0086

Table 4
Cross-sectional areas and thicknesses of tensile specimens.

Plate\Coupon		0-1	0-2	0-3	45-1	45-2	45-3	90-1	90-2	90-3	Avg.	Std. Dev.
HT-T4	Area (mm^2)	49.2	49.6	49.7	49.5	49.7	49.7	49.5	49.4	49.6	49.5	0.16
	Thickness (mm)	3.95	4.01	4.03	3.99	4.02	4.01	3.98	3.99	4.00	4.00	0.02
VL-T4	Area (mm^2)	48.0	47.0	47.3	45.4	46.8	47.7	47.9	47.0	48.2	47.3	0.81
	Thickness (mm)	3.87	3.76	3.80	3.66	3.77	3.84	3.86	3.81	3.88	3.81	0.07
VS-T4	Area (mm^2)	48.8	49.0	49.0	50.3	49.9	49.4	50.3	50.8	50.7	49.8	0.73
	Thickness (mm)	3.93	3.94	3.92	4.07	4.03	3.97	4.05	4.08	4.08	4.01	0.06
VS-T8	Area (mm^2)	119.0	119.1	118.7	119.6	119.5	119.9	117.7	121.2	122.6	119.7	1.36
	Thickness (mm)	7.93	7.94	7.91	8.02	8.01	8.03	7.95	8.13	8.20	8.01	0.09

were considered to acquire the tensile strain of the specimens: 1) two strain gauges measured the strain data parallel and perpendicular to the loading direction at the specimen centre before 20000 $\boldsymbol{\mu\varepsilon}$, as shown in Fig. 8; 2) an extensometer with a standard gauge length of 50 mm measured the elongation during the tensile loading process; 3) an Imetrum digital image correlation (DIC) system measured the specimen elongation and strain field in the entire area. The tensile test setup is shown in Fig. 9.

Fig. 10(a) displays the initial range of stress-strain curves for Coupon VL-T4-0-2 obtained using the three measurement methods. The strain gauge produced the smoothest stress-strain curve, while the others fluctuated considerably. Fig. 10(b) shows the full-range stress-strain curves for Coupon VL-T4-90-1 obtained using the three measurement methods. The strain measured by DIC was larger than that measured by the extensometer due to relative sliding between the extensometer and the coupon surface, resulting in a lower strain measurement than its true value. The DIC measurement was deemed more accurate because it was conducted on the specimens without contact with the surface. Therefore, the strain derived from the strain gauge and DIC were used as the data sources for the stress-strain curves at the initial ($\varepsilon \leq 0.005$) and subsequent ranges ($\varepsilon > 0.005$), respectively. Basic mechanical properties, such as Young's modulus, yield and ultimate strengths, ultimate and fracture strains, and Poisson's ratio were then determined from the stress-strain curves. Since the stress-strain curves contained experimental noise, the finite difference approach was inappropriate for

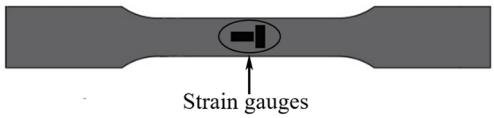

Fig. 8. Strain gauge set-up.

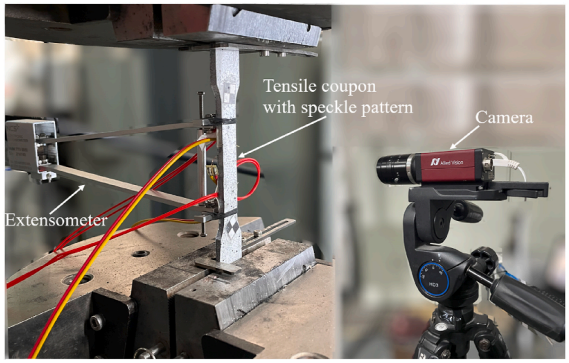

Fig. 9. Tensile test set-up.

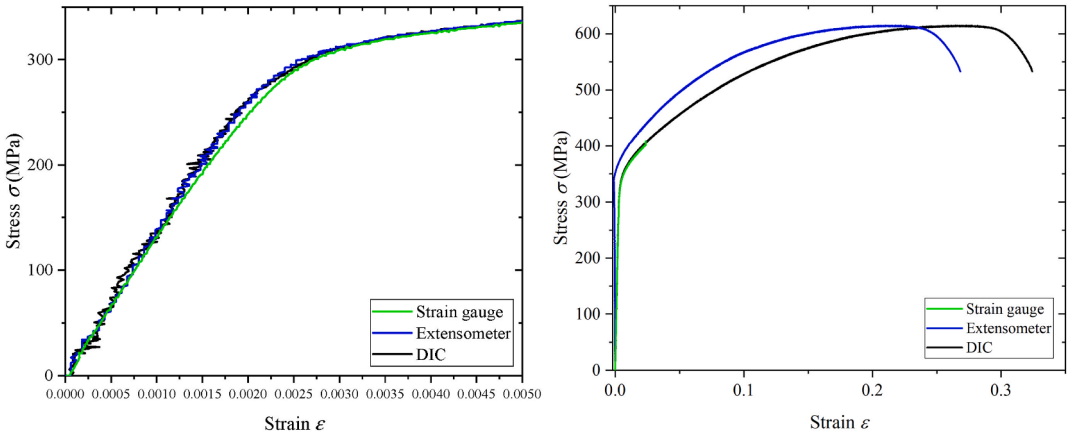

Fig. 10. Comparison between stress-strain curves derived from different methods.

determining Young's modulus. Instead, a moving regression filter was passed to the curve, performing ordinary least squares regression (OLSR) analysis to calculate the derivative corresponding to each point. Young's modulus was then determined from the derivative-strain curve [24]. Poisson's ratio was calculated using the strain data within 1000 $\mu\varepsilon$ to ensure that the specimen was in its elastic stage.

3.3. Fracture surface SEM test and metallographic scanning test

One cube sample was extracted from the excess materials of each of the four deposition plates and prepared for metallographic analysis. The preparation process involved embedding using a metallographic inlaying machine, polishing using sandpaper and the polishing machine to achieve a mirror surface, and etching using an austenitic stainless steel etching solution to reveal their metallographic structure [38]. A CX40 M optical microscope was used for metallographic analysis. Fracture surface SEM test of the coupons and metallographic scanning test of material were performed. Samples for the fracture surface SEM test were prepared, and a QUANTAFEG65 SEM was used to examine the fracture morphology and explore the fracture mechanism.

4. Test results

4.1. Stress-strain curves and mechanical properties

The full range and initial range of the stress-strain curves of the tensile coupons are presented in Figs. 11–14, which were obtained using the method described in Section 3.2. For specimens extracted from plate HL-T4 and VL-T4, the stress-strain curves were very similar for the three coupons in each group (Figs. 11 and 12). However, for specimens extracted from plate VS-T4 and VS-T8, the stress-strain curves for the three coupons in each group were highly dispersed, as shown in Fig. 13–14.

Table 5 presents the average values and standard deviations of the mechanical properties for each group of tensile specimens, including Young's modulus (E), 0.2% proof stress ($\sigma_{0.2}$), ultimate tensile stress (σ_u), yield to ultimate strength ratio ($\sigma_{0.2}/\sigma_u$), ultimate strain (ε_u), fracture strain (ε_f) and Poisson's ratio (ν).

The bar charts of mechanical properties are shown in Fig. 15. As shown in Fig. 15(a), the average Young's modulus varied significantly between groups, ranging from 118.66 to 216.37 GPa. Group VL-T4-45 had the highest average Young's modulus, while Group

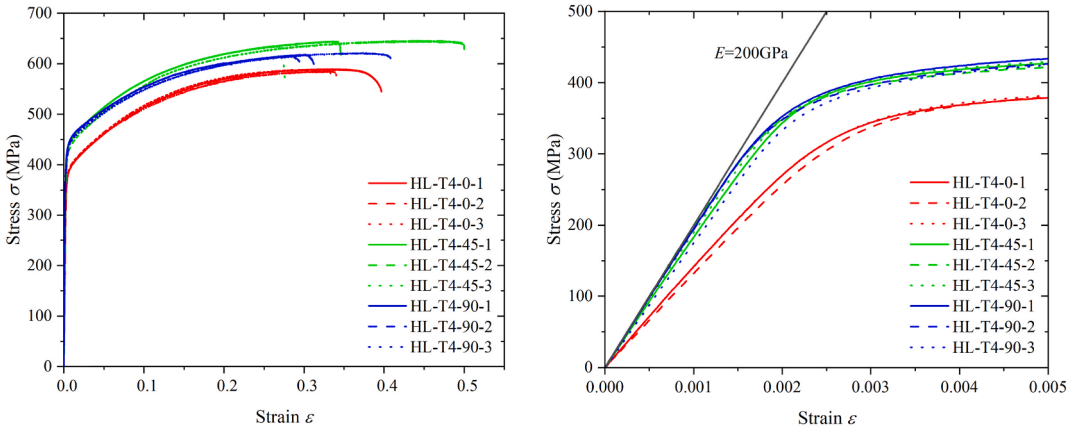

Fig. 11. Stress-strain curves of tensile coupons extracted from plate HL-T4.

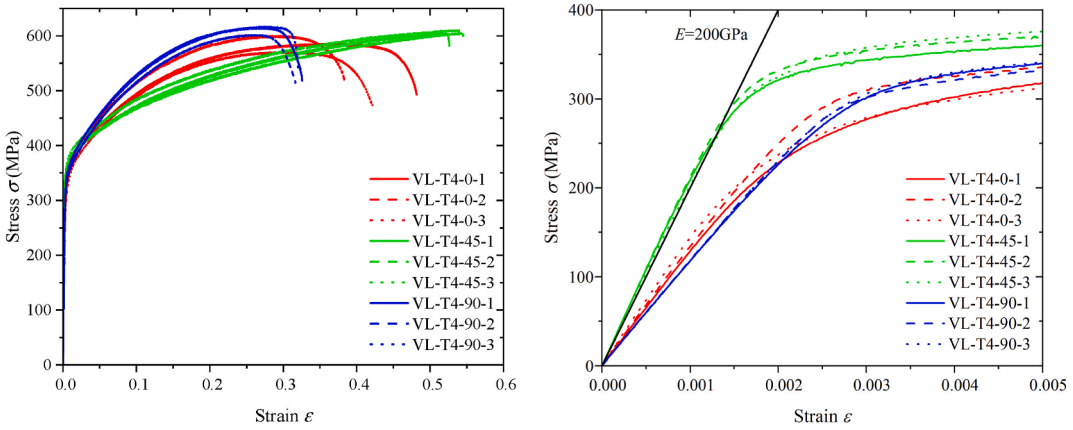

Fig. 12. Stress-strain curves of tensile coupons extracted from plate VL-T4.

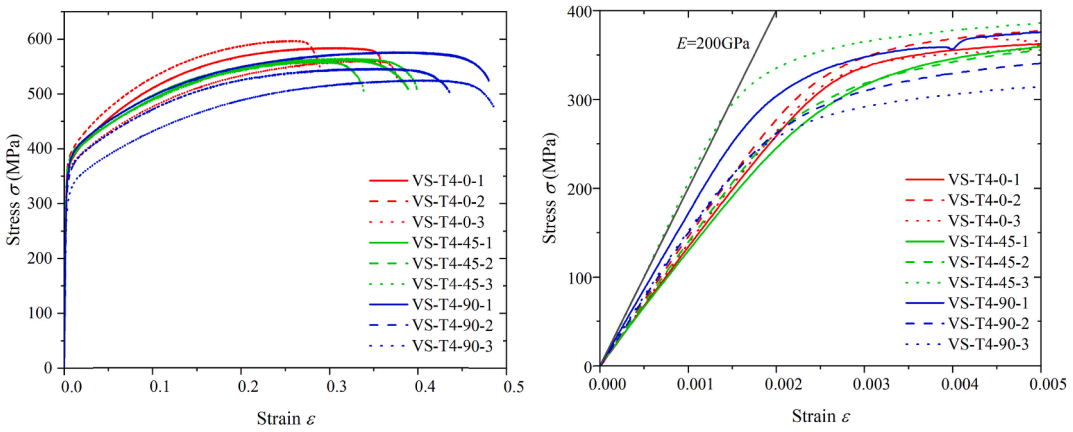

Fig. 13. Stress-strain curves of tensile coupons extracted from plate VS-T4.

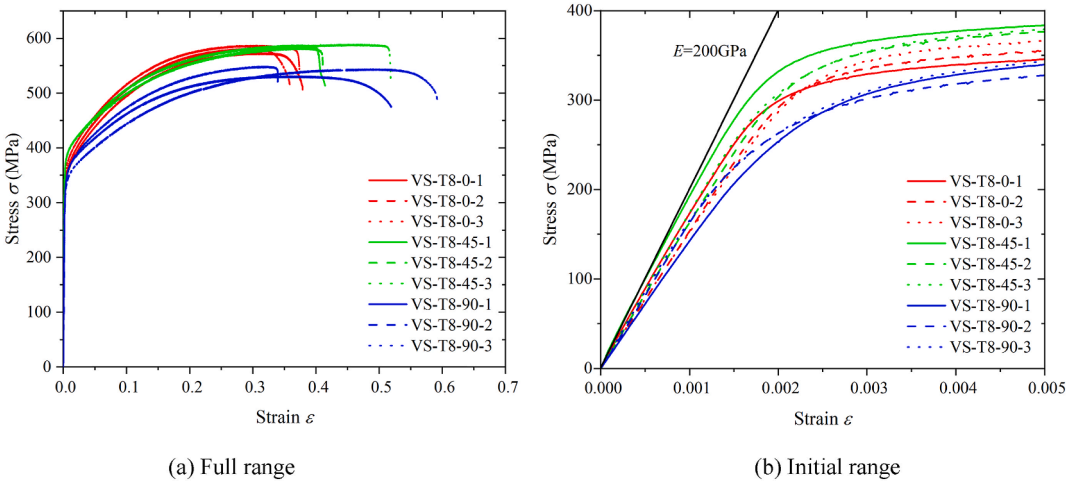

Fig. 14. Stress-strain curves of tensile coupons extracted from plate VS-T8.

Table 5
Mean value and standard deviation of mechanical properties.

Coupon	E/GPa		$\sigma_{0.2}$/MPa		σ_u/MPa		$\sigma_{0.2}/\sigma_u$		ε_u		ε_f		ν	
	$\bar{E}$	σ	$\bar{\sigma}_{0.2}$	σ	$\bar{\sigma}_u$	σ	$\overline{\sigma_{0.2}/\sigma_u}$	σ	$\bar{\varepsilon}_u$	σ	$\bar{\varepsilon}_f$	σ	$\bar{\nu}$	σ
HL-T4-0	140.12	6.28	377.39	1.99	587.97	2.25	0.64	0.01	0.33	0.01	0.36	0.03	0.30	0.01
HL-T4-45	191.17	7.59	419.39	4.65	641.00	6.43	0.65	0.01	0.35	0.09	0.37	0.12	0.20	0.03
HL-T4-90	187.69	11.05	421.29	4.42	617.96	3.45	0.68	0.01	0.32	0.05	0.34	0.06	0.39	0.02
VL-T4-0	139.09	9.37	312.53	15.71	603.31	17.51	0.52	0.02	0.31	0.04	0.43	0.06	0.36	0.02
VL-T4-45	216.37	6.50	359.03	8.51	606.91	3.28	0.59	0.01	0.53	0.01	0.54	0.01	0.11	0.04
VL-T4-90	118.66	0.80	335.98	5.39	611.24	7.97	0.55	0.00	0.27	0.01	0.33	0.01	0.38	0.02
VS-T4-0	139.40	6.28	364.77	8.25	580.68	18.33	0.63	0.01	0.30	0.05	0.35	0.04	0.24	0.07
VS-T4-45	160.29	44.08	360.56	13.32	561.90	2.73	0.64	0.03	0.31	0.01	0.39	0.03	0.26	0.04
VS-T4-90	160.81	10.18	341.50	19.17	549.30	25.82	0.62	0.02	0.38	0.02	0.48	0.03	0.27	0.06
VS-T8-0	161.25	14.81	350.20	11.81	580.54	7.02	0.60	0.01	0.30	0.01	0.38	0.01	0.17	0.05
VS-T8-45	181.61	19.92	372.75	2.23	586.19	3.52	0.64	0.00	0.41	0.05	0.45	0.06	0.16	0.10
VS-T8-90	162.44	16.00	326.21	8.39	541.13	9.21	0.60	0.02	0.39	0.09	0.49	0.13	0.43	0.06

VL-T4-90 had the lowest. The standard deviation of Young's modulus for groups HL-T4-0/45/90 and VL-T4-0/45/90 was smaller than that for groups VS-T4-0/45/90 and VS-T8-0/45/90. Plate VL-T4 exhibited the highest degree of anisotropy, with Group VL-T4-45 having the highest average Young's modulus. Notably, plate VL-T4 was fabricated with the same printing path as Laghi's study [16], and both studies reached similar conclusions regarding the anisotropy of Young's modulus. Plate HL-T4 displayed similar anisotropy but was less distinct than plate VL-T4. Anisotropy is due to the oriented crystal caused by grain growing tracking the highest thermal gradient [24]. Plate HL-T4 was printed in contact with the substrate plate on one side, while plate VL-T4 was printed in contact with air on both sides. Due to the higher thermal conductivity of steel compared to air, the thermal gradient within plate HL-T4 was lower, resulting in a less strong crystallographic texture. Therefore, plate HL-T4 exhibited less distinct anisotropy.

Fig. 15(b) and (c) display the bar charts of average yield strength ($\sigma_{0.2}$) and ultimate strength (σ_u) for all groups, respectively. The yield strength ranged from 312.53 to 421.29 MPa, while the ultimate strength ranged from 541.13 to 641.00 MPa. Groups HL-T4-0/45/90 had higher yield strength than the remaining groups and exhibited relatively smaller dispersion among the three coupons in the same group. The ultimate strength of groups HL-T4-0/45/90 and VL-T4-0/45/90 was slightly higher than the other groups. The anisotropy of yield strength and ultimate strength was not distinct for the four plates.

As shown in Fig. 15(d) and (e), the ultimate strain ranged from 0.27 to 0.53, and the fracture strain ranged from 0.33 to 0.54. Plate VL-T4 exhibited the most distinct anisotropy in both ultimate and fracture strains, with the order being VL-T4-45 > VL-T4-0 > VL-T4-90.

As shown in Fig. 15(f), Poisson's ratio exhibited considerable anisotropy in plates VL-T4 and HL-T4, which followed the order of VL-T4-90 > VL-T4-0 > VL-T4-45 and HL-T4-90 > HL-T4-0 > HL-T4-45. In these two plates, the Poisson's ratio of the 90° (groups VL-T4-90 and HL-T4-90) and 0° (groups VL-T4-0 and HL-T4-0) coupons ranged from 0.3 to 0.4, whereas those of the 45° coupons was no more than 0.2. The magnitudes of Poisson's ratio are similar to the results of Laghi's study [21]. Laghi et al. [21] also found that the symmetry condition $E_0 \bullet \nu_0 \approx E_{90} \bullet \nu_{90}$ existed in WAAM sheet material, indicating orthotropic material behaviour. This condition was also applicable to plate HL-T4 but not to plate VL-T4 in this study. Poisson's ratio exhibited considerable dispersion among coupons in each group in plates VS-T4 and VS-T8. Thus, it had little reference value.

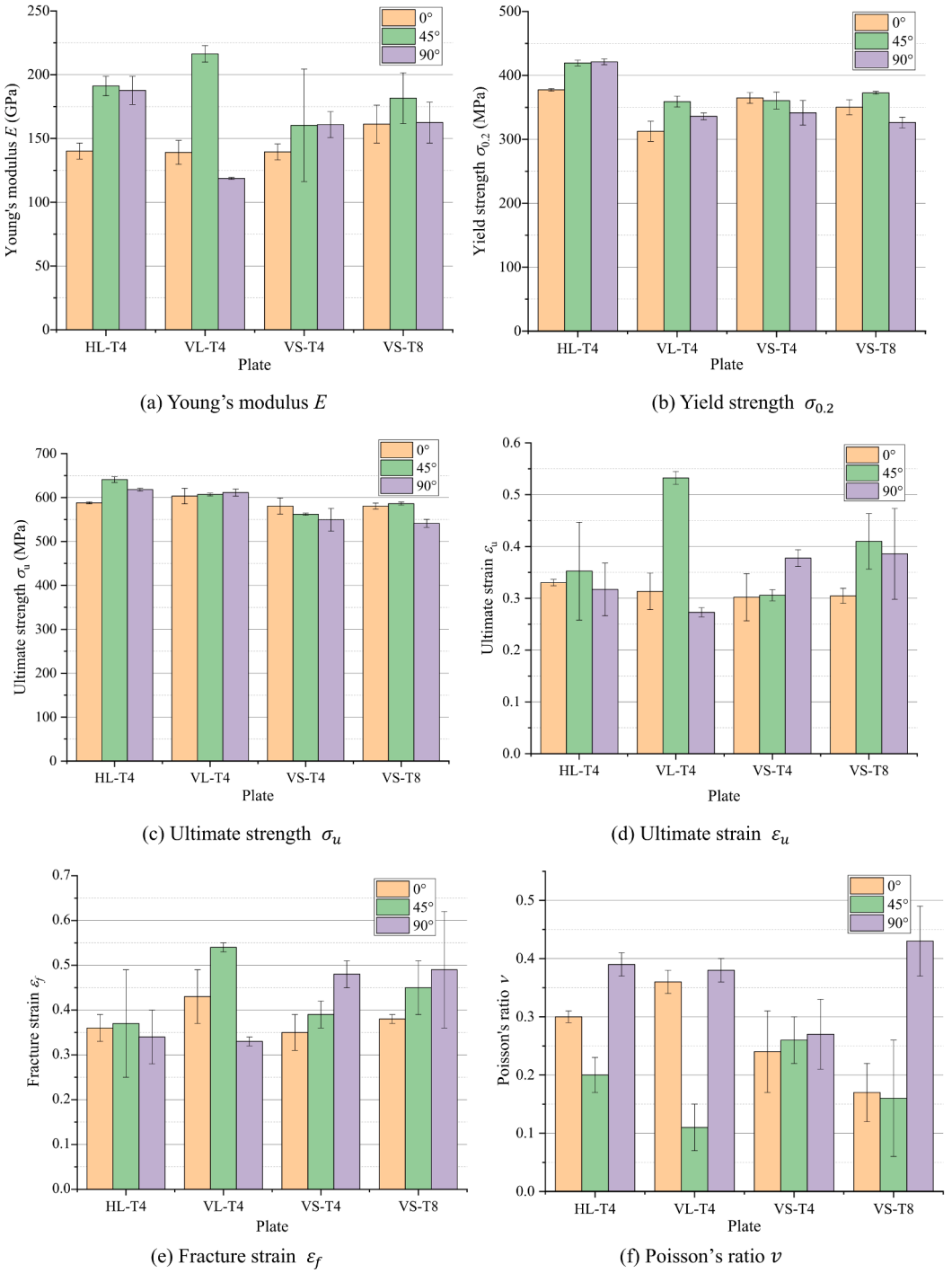

(a) Young's modulus E (b) Yield strength $\sigma_{0.2}$

(c) Ultimate strength σ_u (d) Ultimate strain ε_u

(e) Fracture strain ε_f (f) Poisson's ratio ν

Fig. 15. Mean value and standard deviation of mechanical properties.

Fig. 16 displays the typical macroscopic fracture surfaces of each group of specimens. Specimens from Groups VL-T4-45 and HL-T4-45 exhibited diagonal stripes, as shown in Fig. 16(b) and (e). This indicates slip dislocation between the printing layers, resulting in a higher yield and fracture strain. Necking phenomena were observed in specimens from Groups VL-T4-0, VS-T4-90 and VS-T8-90, as shown in Fig. 16(d), (i) and (l), which also resulted in higher fracture strain. Specimens from Groups HL-T4-90 and VL-T4-90 had stripes perpendicular to the loading direction, suggesting incomplete infusion between printing layers, as shown in Fig. 16(c) and (f), which results in the lowest fracture strain among the three sampling discretions.

The test results obtained in this study were compared with previous studies [18,19,39–41] and related standards [42–44], as shown in Table 6. The mechanical properties obtained in this study were comparable to those obtained in previous studies. The yield

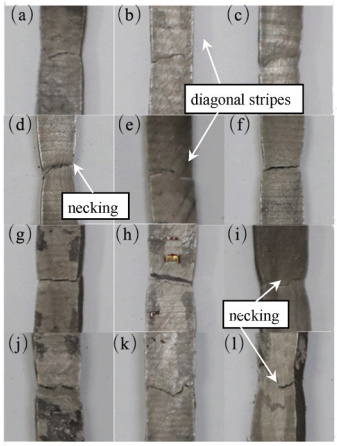

(a) HL-T4-0; (b) HL-T4-45; (c) HL-T4-90; (d) VL-T4-0; (e) VL-T4-45; (f) VL-T4-90; (g) VS-T4-0; (h) VS-T4-45; (i) VS-T4-90; (j) VS-T8-0; (k) VS-T8-45; (l) VS-T8-90

Fig. 16. Typical macroscopic fracture morphology for each group of specimens.

Table 6
Summary of mechanical properties of WAAM stainless steel.

References	Technique	Material	Sampling mode	Yield strength $\sigma_{0.2}$ (MPa)	Ultimate strength σ_u (MPa)	Fracture strain ε_f (%)
Chen et al. [19]	GMAW	316L	VL-R2.5-90	235 ± 6	533 ± 23	48 ± 2
Wang et al. [18]	CMT	316L	HL-T2-0	384.8	563.1	28.42
			HL-T2-90	382.8	555.1	37.25
			VL-T2-0	394.1	577.5	41.87
			VL-T2-90	361.3	526.9	46.24
			VS-T2-0	400.6	586.9	28.45
			VS-T2-90	346.5	545.3	31.06
Rodriguez et al. [40]	CMT	316L	VL-T4-0	364 ± 14	577 ± 4	43 ± 5
			VL-T4-90	337 ± 2	574 ± 8	42 ± 4
Sasikumar et al. [41]	GMAW	316L	VL-T1-0	262.10	579.73	34.30
			VL-T1-90	252.00	675.77	39.41
Cast 316L [44]		316L	-	262	552	55
Wrought 316L (cold finished) [44]		316L	-	255–310	525–623	30
Wrought 316L (Heat treatment-annealing) [44]		316L	-	170	480	40
Standard (China) [43]		316L	-	180	485	40
Standard (USA) [42]		316L	-	170	450	40

strength and ultimate strength of the specimens in this study were approximately 2 times and 1.2 times those of the national standard of 316L stainless steel, respectively. However, only Groups VL-T4-0, VL-T4-45, VS-T4-90, VS-T8-45 and VS-T8-90 met the fracture strain requirements stipulated by the standards. Group VL-T4-90 had the lowest fracture strain, which was approximately 80% of the standard requirement.

4.2. Metallographic structure

A cube sample was extracted from each of the four deposition plates to observe the metallographic structure of the material using a CX40 M optical microscope. Fig. 17 shows the metallographic morphologies of the four samples. The metallographic structure consisted of regular polygonal grains with distinct and straight boundaries, which were typical of austenitic metallography. Moreover, the grain size varied among the plates: Plates HL-T4 had the smallest grains, VL-T4 had intermediate grains, and plates VS-T4 and VS-T8 had large grains.

Previous studies also reported larger grain sizes in oscillated walls (corresponding to plate VS-T4 and VS-T8 in this study) than in single-pass walls (corresponding to plate HL-T4 and VL-T4 in this study) [29,30]. This is due to the lower cooling rate of the former printing strategy. For a given position, it takes less time for the torch to move to the same position in the next layer for the 'VS' (or oscillated) printing strategy, resulting in the accumulation of heat input. Therefore, the grain size was larger in plates VS-T4 and VS-T8 than in plates HL-T4 and VL-T4. Plate HL-T4 was printed in contact with the substrate plate on one side, while plate VL-T4 was printed in contact with air on both sides. Due to the higher thermal conductivity of steel compared to air, the cooling rate of plate HL-T4 was higher than that of VL-T4, resulting in a finer grain in plate HL-T4 than in VL-T4.

The grain size is correlated with yield and ultimate strengths. As grain size decreases, the number of grain boundaries increases, impeding dislocation motion with the formation of dislocation pile-up and resulting in enhanced yield and ultimate strengths but de-

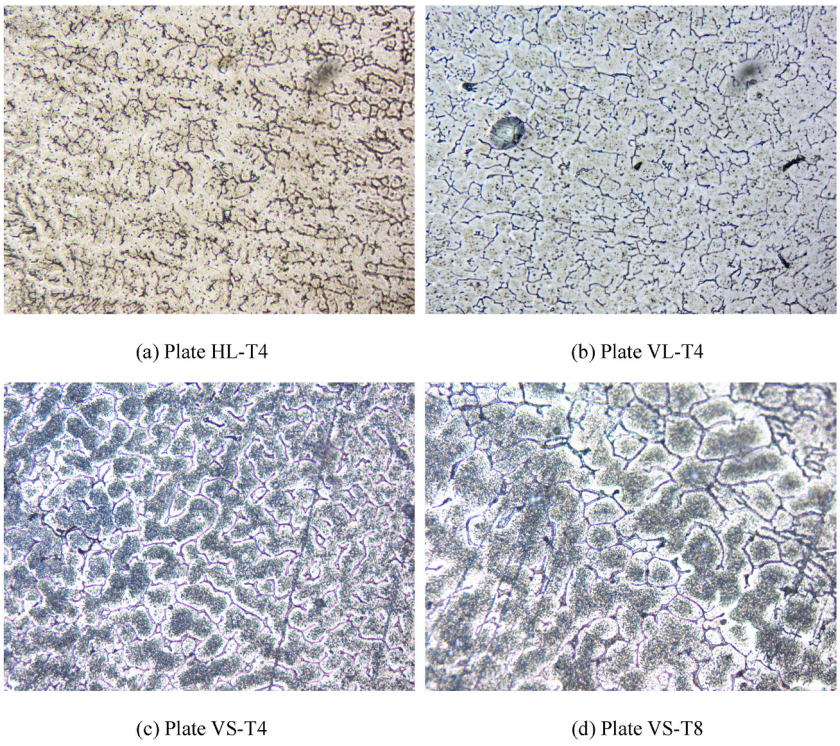

(a) Plate HL-T4 (b) Plate VL-T4

(c) Plate VS-T4 (d) Plate VS-T8

Fig. 17. Metallographic microstructure in OM.

creased ductility [45–48]. This explains the magnitude order of yield and ultimate strengths of specimens among different plates except for plate VL-T4. However, specimens from plate VL-T4 exhibited the lowest yield strength and high ductility despite its relatively small grain size. This was likely due to its highly uniform grain orientation, which facilitated dislocation and increased its capacity for plastic deformation.

4.3. Microscopic morphology of fracture surfaces

For all specimens, the morphology of each fracture surface varied significantly across different areas. However, most areas exhibited dimples, a typical feature of transgranular plastic fracture [49], indicating a ductile fracture mechanism. As shown in Fig. 18, the smallest dimples were found in specimens from plates HL-T4, followed by plates VL-T4. Specimens from plates VS-T4 and VS-T8, particularly VS-T4-90 and VS-T8-90, had relatively large dimples. The dimple size is positively related to the grain size [50]. Large-sized dimples are generally caused by severe plastic deformation, indicating high ductility [50–52]. The dimple size observed was consistent with grain size and ductility for each plate.

The fracture surfaces were predominantly dimpled, but some cleavages were also observed. Cleavage, a characteristic feature of brittle fracture morphology [53], results from stress concentration caused by the excessive thermal gradient between layers and non-uniform cooling during the manufacturing process [54]. Many river-shaped cleavages were found on the fracture surfaces of Coupon HL-T4-45-3 and VS-T8-90-3, as shown in Fig. 19, suggesting that these specimens experienced both ductile and brittle fractures in different regions. This resulted in the relatively lower ductility for these two specimens compared to the others in their group, as shown in Figs. 11 and 14.

Inclined dimples were observed on fracture surfaces of group HL-T4-90, VL-T4-90, VS-T4-0/45/90 and VS-T8-0/45/90, as shown in Fig. 20. Normal stress forms equiaxed dimples, while shear stress causes microscopic holes to grow faster along the shear direction, forming parabolic or semi-elliptical dimples. The dimples on the two mating fracture surfaces face opposite directions for shear dimples and the same direction for tear dimples. The observed inclined dimples were formed due to the tearing of the specimens perpendicular to the loading direction. This might be caused by incomplete fusion between printing layers, which were perpendicular to the loading directions in these groups of specimens.

Step-shaped morphologies were observed on the fracture surfaces of groups VL-T4-45 and HL-T4-45, as shown in Fig. 21, indicating slip dislocation between the deposition layers under the tensile load. This caused a relatively larger elongation of these two groups. Slip dislocation occurred because the printing layers were parallel to the direction of the largest shear stress in these two groups.

A few defects were observed, such as incompletely melted wires and balls, and pores, as shown in Fig. 22. Fluctuations in process parameters, scanning trajectory and external environment led to internal defects in materials [55], which affected the microstructure, mechanical properties, and service safety of structural components.

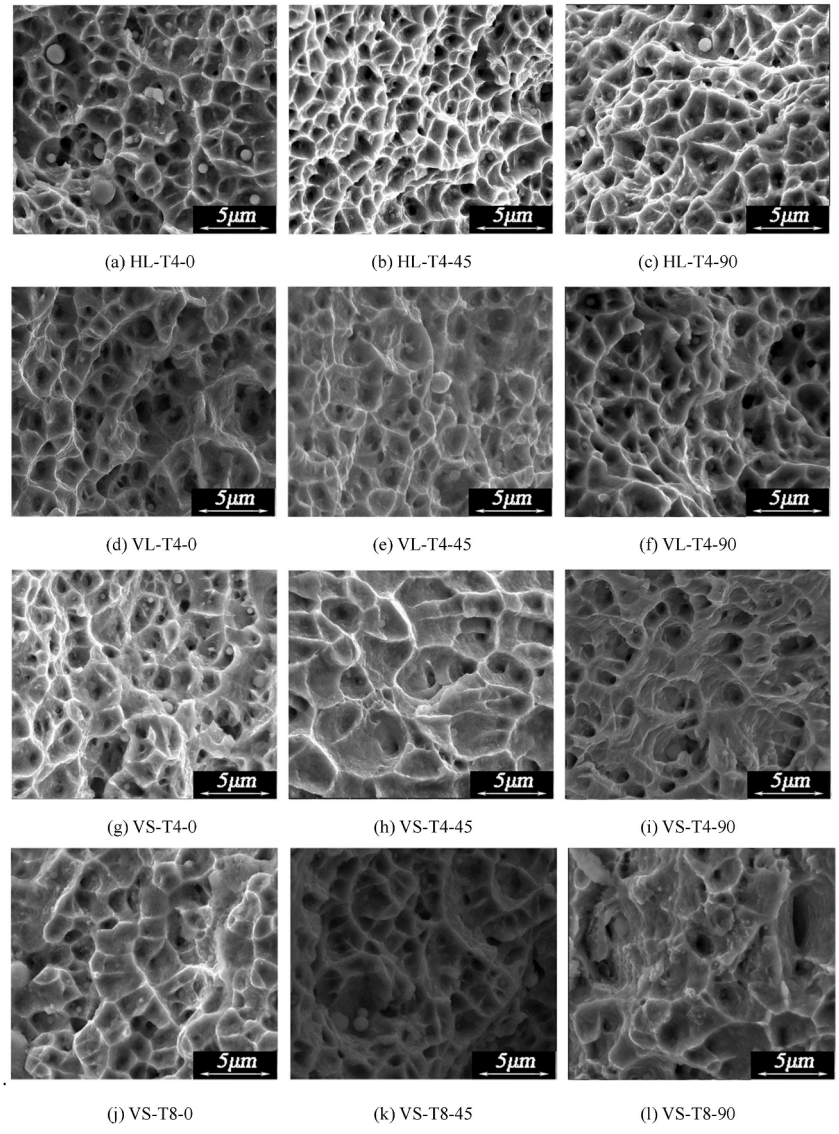

Fig. 18. Dimple morphology on fracture surfaces for each group of specimens.

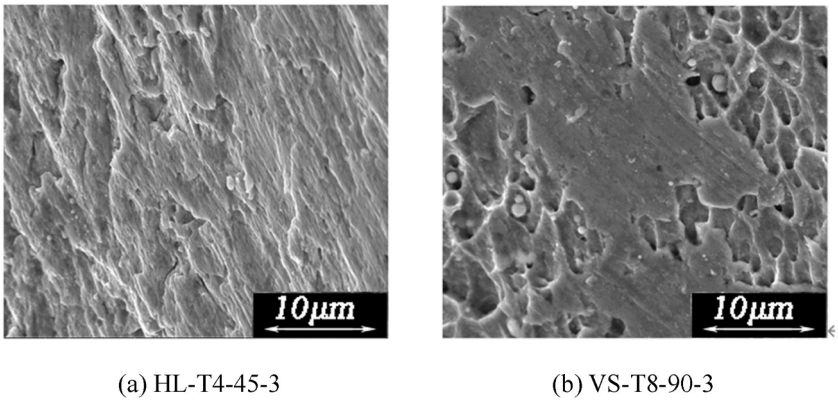

Fig. 19. Cleavages on fracture surfaces.

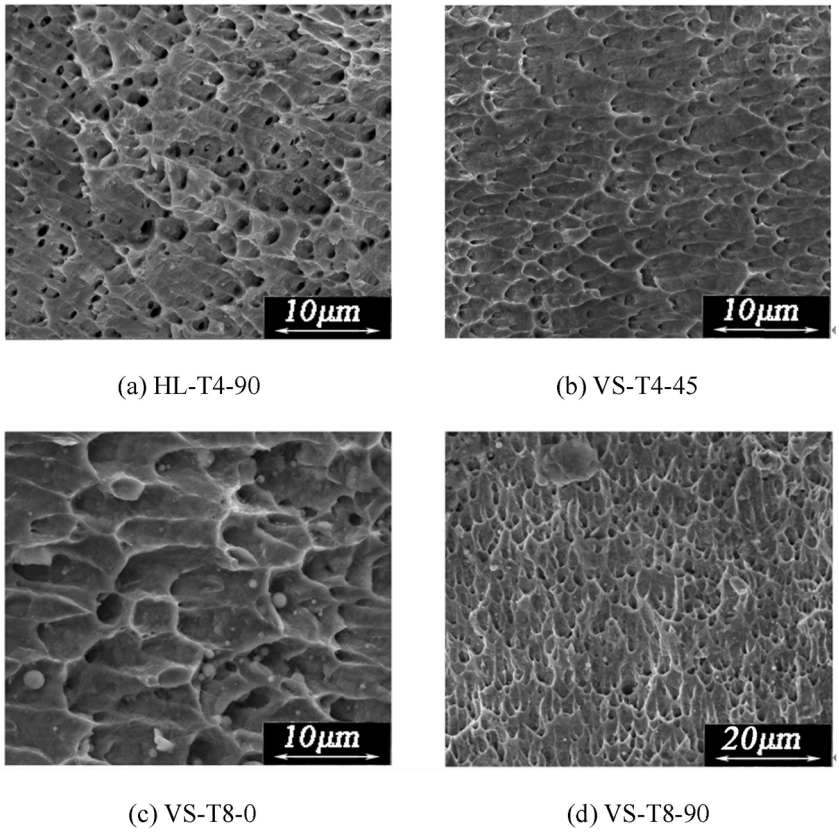

Fig. 20. Inclined dimples on fracture surfaces.

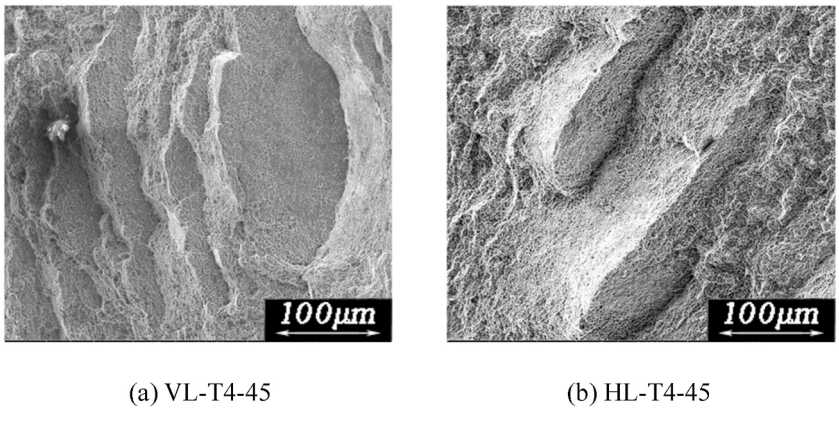

Fig. 21. Step-shaped morphologies.

5. Effect of heat treatment on the mechanical properties

The mechanical properties obtained in this study were compared with those of materials after solution heat treatment to examine the effects of heat treatment on the mechanical properties. The comparison data was obtained from our previous study [56], which used the same set of process inputs for manufacturing, the same specimen sampling method, and the same experimental procedures as this study, except that heat treatment was performed on the material. The heat-treated specimens were heated to 1050 °C at a rate of 4–6 °C/min, and then air quenched and rapidly cooled after being maintained for 2 h.

Solution heat treatment is an essential method for metal processing. The carbide dissolves in the matrix when heated to around 1100 °C, and homogeneously distributes in it after holding for enough time. The homogeneous distribution of carbide improves the corrosion resistance and ductility of the steel [57]. Moreover, the grain size increases and become relatively uniform, and sub-grains and dislocations are eliminated. As a result, the solution heat treatment reduces the yield and ultimate strengths but enhances the ductility [57–60].

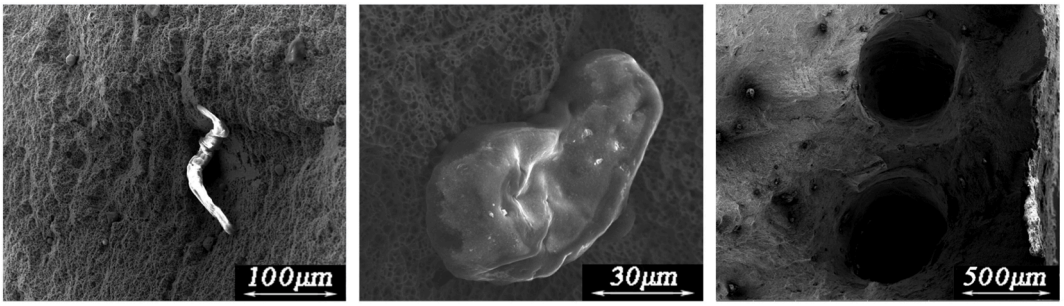

Fig. 22. Defects on fracture surfaces.

The mechanical properties of the solution heat-treated tensile coupons are shown in Table 7. Figs. 23 and 24 compare the mechanical properties of the heat-treated and untreated tensile coupons. Young's modulus is almost identical because it is a stable property of the material that does not depend on the processing method.

As shown in Table 7, solution heat treatment significantly reduced the yield and ultimate strengths of the tensile coupons. The heat-treated coupons had a yield strength range of 240–298 MPa, and an ultimate strength range of 473–618 MPa, which were approximately 30% and 17% lower, respectively, than those of unheated counterparts. The yield-to-ultimate strength ratio of the heat-treated coupons also decreased significantly and became more uniform between different groups. The fracture strain of the heat-treated coupons ranged from 0.41 to 0.59, which was 10–70% higher than that of the untreated coupons except for one group (VL-T4-

Table 7
Mean value and standard deviation of mechanical properties (heat treatment) [56].

Coupon	E/GPa		$\sigma_{0.2}$/MPa		σ_u/MPa		$\sigma_{0.2}/\sigma_u$		ε_f		μ	
	$\bar{E}$	σ	$\bar{\sigma}_{0.2}$	σ	$\bar{\sigma}_u$	σ	$\bar{E}$	σ	$\bar{\sigma}_{0.2}$	σ	$\bar{\sigma}_u$	σ
HL-T4-0	145.86	18.93	262	2.36	529	3.74	0.49	0	0.45	0.02	0.29	0.03
HL-T4-45	216.54	43.04	287	1.25	582	4.97	0.49	0.01	0.51	0.03	0.26	0.02
HL-T4-90	198.2	33.16	286	1.25	568	1.25	0.5	0	0.54	0.03	0.36	0.07
VL-T4-0	137.21	7.84	268	6.16	537	8.38	0.5	0	0.48	0.01	0.4	0.02
VL-T4-45	198.07	8.84	298	6.6	618	16.42	0.48	0	0.50	0.01	0.09	0.01
VL-T4-90	144.6	6.12	262	4.97	506	2.49	0.52	0.01	0.57	0.04	0.44	0.01
VS-T4-0	158.71	11.85	263	4.5	529	2.5	0.5	0.01	0.41	0.00	0.35	0.02
VS-T4-45	185.71	12.91	266	1.7	527	6.55	0.5	0	0.58	0.01	0.17	0.05
VS-T4-90	161.73	11.72	260	5.89	515	2.49	0.5	0.01	0.59	0.03	0.3	0.06
VS-T8-0	154.34	5.07	260	6.13	523	2.16	0.5	0.01	0.44	0.03	0.45	0.09
VS-T8-45	150.71	5.68	258	2.87	509	4.5	0.51	0	0.52	0.04	0.38	0.04
VS-T8-90	184.27	17.37	240	5.79	473	1.7	0.51	0.01	0.53	0.01	0.1	0.06

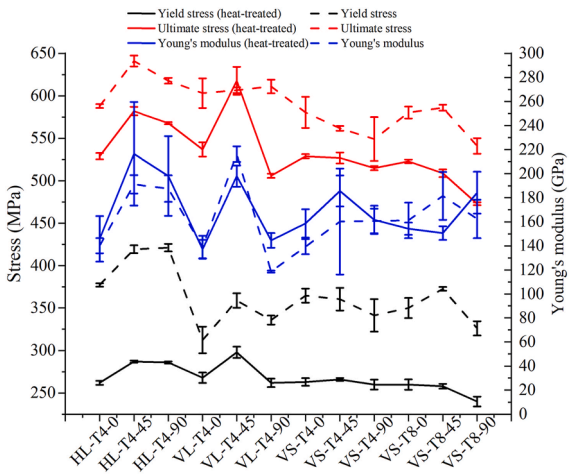

Fig. 23. Comparison of the yield strength, ultimate strength, and Young's modulus between heat-treated and untreated specimens.

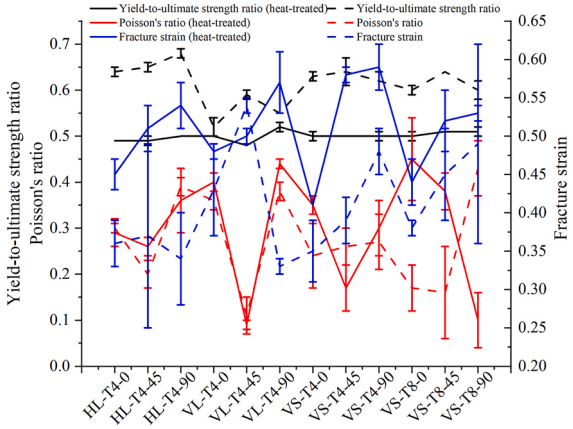

Fig. 24. Comparison of yield-to-ultimate strength ratio, Poisson's ratio, and fracture strain between heat-treated and untreated specimens.

45). In the case of tensile coupons extracted from Plates HL-T4 and VL-T4, the Poisson's ratios were similar between coupons with and without heat treatment. As mentioned above, solution heat treatment enhances the ductility and reduces the strength of WAAM 316L stainless steel by increasing the grain size and the homogeneous distribution of carbide. This existing knowledge was consistent with the experimental results in this study.

6. Conclusions

In this paper, four 316L stainless steel deposition plates were fabricated using the CMT-WAAM technique with different printing paths, and nine tensile specimens were extracted from each plate in three different directions (0°, 45° and 90° to the long side of plate). Tensile tests were conducted to obtain insight into the mechanical properties of WAAM material. The effect of printing paths was investigated by comparing the mechanical behaviours and microstructures of coupons extracted from the four plates. Anisotropy was investigated by testing coupons extracted from different directions. The metallographic structure and fracture surface morphology were observed and analysed using OM and SEM respectively, and the correlation between mechanical properties and microstructures was explored. The effect of heat treatment was investigated by comparing the mechanical properties of heat-treated and untreated materials. The main results are as follows:

(1) The results of tensile tests demonstrated that the yield and ultimate strengths of the coupons were comparable to previous studies and met the requirements of the relevant standards. However, the fracture strain was slightly lower than that specified by relevant standards. Plate HL-T4 exhibited the highest yield and ultimate strengths and lowest fracture strain, while plate VL-T4 exhibit the lowest yield strength and relatively high fracture strain, especially in the 45° sampling direction.
(2) Anisotropy was observed in plate HL-T4 and VL-T4 but was less pronounced in plate HL-T4. The Young's modulus, ultimate strain and fracture strain exhibited the highest value in the 45° specimens, while the ultimate strength did not exhibit anisotropy. Plate VS-T4 and VS-T8 did not exhibit anisotropy.
(3) The metallographic analysis demonstrated that the microstructure was austenitic. The grain sizes of the plates followed the order: HL-T4 < HL-T8 < VS-T4 and VS-T8. The variation in grain size among different plates was due to the different heat inputs of different printing paths. Overall, plates with finer grains exhibited higher strength but lower ductility, except for plate VL-T4, which was likely due to the highly uniform grain orientation which facilitated plastic deformation.
(4) Fracture surface SEM test demonstrated that the morphology of the fracture surface was mainly composed of dimples, indicating a ductile fracture mechanism. The dimple size was positively correlated with the grain size. Overall, large dimples were associated with high ductility. The fracture surfaces of coupons in groups VL-T4-45 and HL-T4-45 exhibited a step-shaped morphology, indicating slip dislocation, which resulted in large ductility in these cases. Some cleavages were observed, suggesting a combination of ductile and brittle fractures, resulting in reduced ductility in several specimens. Inclined dimples formed due to tearing between the printing layers of the coupons with printing layers perpendicular to the loading direction. In addition, a large number of defects were observed, including pores and un-melted wires.
(5) A few mechanical properties of the materials were changed after solution heat treatment. Compared to untreated specimens, the yield strength and ultimate strength of the heat-treated specimens decreased by approximately 30% and 17%, respectively, while the fracture strain increased by 10–70%. Heat treatment had little effect on Young's modulus.

Author contribution statement

Yang Zhao: Writing – review & editing, Supervision, Resources, Project Administration, Funding Acquisition, Conceptualization. Yin Chen: Writing – review & editing, Methodology, Investigation. Zhen Wang: Writing – review & editing, Supervision. Jun Ye: Writing – review & editing, Supervision, Resources, Funding Acquisition, Conceptualization. Weijian Zhao: Writing – review & editing.

Declaration of competing interest

There is no conflict of interest among the authors in the manuscript.

Data availability

Data will be made available on request.

Acknowledgement

The authors would like to acknowledge the project supported by the National Natural Science Foundation of China (No.52078452, 52208215), and the Basic Public Research Project of Zhejiang Province (No. LGG22E080005, LQ22E080008).

References

[1] ISO/ASTM 52900, Additive Manufacturing -- General Principles -- Fundamentals and Vocabulary, A. International, West Conshohocken, PA., 2021.
[2] L. Gardner, Metal additive manufacturing in structural engineering – review, advances, opportunities and outlook, Structures 47 (2023) 2178–2193.
[3] S.H. Huang, P. Liu, A. Mokasdar, L. Hou, Additive manufacturing and its societal impact: a literature review, Int. J. Adv. Manuf. Technol. 67 (2013) 1191–1203.
[4] Y.C. Zhou, Y. Zhao, Tensile properties of additively manufactured 316L stainless steel, China Civ. Eng. J. 53 (2020) 26–35.
[5] A. Puzatova, P. Shakor, V. Laghi, M. Dmitrieva, Large-Scale 3D Printing for Construction Application by Means of Robotic Arm and Gantry 3D Printer: A Review, Buildings.Electronic, 2022.
[6] Y. Zhang, L. Wu, X. Guo, S. Kane, Y. Deng, Y.-G. Jung, J.-H. Lee, J. Zhang, Additive manufacturing of metallic materials: a review, J. Mater. Eng. Perform. 27 (2018) 1–13.
[7] S.W. Williams, F. Martina, A.C. Addison, J. Ding, G. Pardal, P. Colegrove, Wire + Arc Additive manufacturing, Mater. Sci. Technol. 32 (2016) 641–647.
[8] S. Selvi, A. Vishvaksenan, E. Rajasekar, Cold metal transfer (CMT) technology - an overview, Defence Technology 14 (2018) 28–44.
[9] V. Dhinakaran, B. Stalin, M. Ravichandran, M. Balasubramanian, C. Anand Chairman, D. Pritima, Wire Arc additive manufacturing perspectives and recent developments, IOP Conf. Ser. Mater. Sci. Eng. 988 (2020) 012102.
[10] L. Gardner, P. Kyvelou, G. Herbert, C. Buchanan, Testing and initial verification of the world's first metal 3D printed bridge, J. Constr. Steel Res. 172 (2020) 106233.
[11] Takenaka MX3D, Connector for Takenaka, Web Page, 2019.
[12] J. Ye, P. Kyvelou, F. Gilardi, H. Lu, M. Gilbert, L. Gardner, An end-to-end framework for the additive manufacture of optimized tubular structures, IEEE Access 9 (2021) 165476–165489.
[13] T. Feucht, B. Waldschmitt, J. Lange, M. Erven, Additive manufacturing of a bridge in situ, Steel Construction 15 (2022) 100–110.
[14] V. Laghi, M. Palermo, L. Tonelli, G. Gasparini, V.A. Girelli, L. Ceschini, T. Trombetti, Mechanical response of dot-by-dot wire-and-arc additively manufactured 304L stainless steel bars under tensile loading, Construct. Build. Mater. 318 (2022) 125925.
[15] L. Tonelli, R. Sola, V. Laghi, M. Palermo, T. Trombetti, L. Ceschini, Influence of interlayer forced air cooling on microstructure and mechanical properties of wire arc additively manufactured 304L austenitic stainless steel, Steel Res. Int. 92 (2021) 2100175.
[16] V. Laghi, M. Palermo, L. Tonelli, G. Gasparini, L. Ceschini, T. Trombetti, Tensile properties and microstructural features of 304L austenitic stainless steel produced by wire-and-arc additive manufacturing, Int. J. Adv. Manuf. Technol. 106 (2020) 3693–3705.
[17] S. Evans, J. Wang, Material properties and local stability of WAAM stainless steel plates with different deposition rates, Int. Conf. Adv. Steel Struc. Conf. Proc. (2022).
[18] C. Wang, T.G. Liu, P. Zhu, Y.H. Lu, T. Shoji, Study on microstructure and tensile properties of 316L stainless steel fabricated by CMT wire and arc additive manufacturing, in: Materials Science and Engineering A-Structural Materials Properties Microstructure and Processing, 2020, p. 796.
[19] X. Chen, J. Li, X. Cheng, B. He, H. Wang, Z. Huang, Microstructure and mechanical properties of the austenitic stainless steel 316L fabricated by gas metal arc additive manufacturing, Mater. Sci. Eng., A 703 (2017) 567–577.
[20] N. Hadjipantelis, B. Weber, C. Buchanan, L. Gardner, Description of anisotropic material response of wire and arc additively manufactured thin-walled stainless steel elements, Thin-Walled Struct. 171 (2022) 108634.
[21] V. Laghi, L. Tonelli, M. Palermo, M. Bruggi, R. Sola, L. Ceschini, T. Trombetti, Experimentally-validated orthotropic elastic model for Wire-and-Arc Additively Manufactured stainless steel, Addit. Manuf. 42 (2021) 101999.
[22] V. Laghi, M. Palermo, G. Gasparini, V.A. Girelli, T. Trombetti, On the influence of the geometrical irregularities in the mechanical response of Wire-and-Arc Additively Manufactured planar elements, J. Constr. Steel Res. 178 (2021) 106490.
[23] V. Laghi, M. Palermo, G. Gasparini, V.A. Girelli, T. Trombetti, Experimental results for structural design of Wire-and-Arc Additive Manufactured stainless steel members, J. Constr. Steel Res. 167 (2020) 105858.
[24] P. Kyvelou, H. Slack, D.D. Mountanou, M.A. Wadee, T. Ben Britton, C. Buchanan, L. Gardner, Mechanical and microstructural testing of wire and arc additively manufactured sheet material, Mater. Des. (2020) 192.
[25] G. van Bolderen, Exploration of Stability of 3D-Printed Steel Members: A Study to Buckling Behaviour of Wire and Arc Additively Manufactured Stainless Steel Tubular Columns, 2017.
[26] V. Laghi, M. Palermo, G. Gasparini, M. Veljkovic, T. Trombetti, Assessment of design mechanical parameters and partial safety factors for Wire-and-Arc Additive Manufactured stainless steel, Eng. Struct. 225 (2020) 111314.
[27] T.A. Rodrigues, J.D. Escobar, J. Shen, V.R. Duarte, G.G. Ribamar, J.A. Avila, E. Maawad, N. Schell, T.G. Santos, J.P. Oliveira, Effect of heat treatments on 316 stainless steel parts fabricated by wire and arc additive manufacturing : microstructure and synchrotron X-ray diffraction analysis, Addit. Manuf. 48 (2021) 102428.
[28] A.S. Yildiz, K. Davut, B. Koc, O. Yilmaz, Wire arc additive manufacturing of high-strength low alloy steels: study of process parameters and their influence on the bead geometry and mechanical characteristics, Int. J. Adv. Des. Manuf. Technol. 108 (2020) 3391–3404.
[29] E. Aldalur, F. Veiga, A. Suárez, J. Bilbao, A. Lamikiz, High deposition wire arc additive manufacturing of mild steel: strategies and heat input effect on microstructure and mechanical properties, J. Manuf. Process. 58 (2020) 615–626.
[30] P. Dirisu, S. Ganguly, A. Mehmanparast, F. Martina, S. Williams, Analysis of fracture toughness properties of wire + arc additive manufactured high strength low alloy structural steel components, Mater. Sci. Eng. 765 (2019) 138285.
[31] X. Xu, J. Ding, S. Ganguly, C. Diao, S. Williams, Preliminary investigation of building strategies of maraging steel bulk material using wire + Arc Additive manufacture, J. Mater. Eng. Perform. 28 (2019) 594–600.
[32] A. Caballero, J. Ding, S. Ganguly, S. Williams, Wire + Arc Additive Manufacture of 17-4 PH stainless steel: effect of different processing conditions on microstructure, hardness, and tensile strength, J. Mater. Process. Technol. 268 (2019) 54–62.
[33] M. Vishnukumar, V. Muthupandi, S. Jerome, Effect of post-heat treatment on the mechanical and corrosion behaviour of SS316L fabricated by wire arc additive manufacturing, Mater. Lett. 307 (2022) 131015.
[34] J.W. Elmer, K. Fisher, G. Gibbs, J. Sengthay, D. Urabe, Post-build thermomechanical processing of wire arc additively manufactured stainless steel for improved mechanical properties and reduction of crystallographic texture, Addit. Manuf. 50 (2022) 102573.
[35] S.I. Evans, J. Wang, J. Qin, Y. He, P. Shepherd, J. Ding, A review of WAAM for steel construction – manufacturing, material and geometric properties, design,

and future directions, Structures 44 (2022) 1506–1522.
[36] T.J. Dodwell, L.R. Fleming, C. Buchanan, P. Kyvelou, G. Detommaso, P.D. Gosling, R. Scheichl, W.S. Kendall, L. Gardner, M.A. Girolami, C.J. Oates, A data-centric approach to generative modelling for 3D-printed steel, Proceedings. Mathematical, physical, and engineering sciences 477 (2021) 20210444.
[37] GB/T 228. 1-2010, Metallic Materials -- Tensile Testing -- Part 1: Method of Test at Room Temperature, CISA, Beijing, 2011.
[38] Z.D. Chen, Proper preparation of metallographic samples, Heat Treatment 37 (2022) 40–45 + 49.
[39] J. Lange, T. Feucht, M. Erven, 3D printing with steel Additive Manufacturing for connections and structures, Steel Construction-Design and Research 13 (2020) 144–153.
[40] N. Rodriguez, L. Vazquez, I. Huarte, I. Arruti, I. Tabernero, P. Alvarez, Wire and arc additive manufacturing: a comparison between CMT and TopTIG processes applied to stainless steel, Weld. World 62 (2018) 1083–1096.
[41] R. Sasikumar, A.R. Kannan, S.M. Kumar, R. Pramod, N.P. Kumar, N.S. Shanmugam, Y. Palguna, S. Sivankalai, Wire arc additive manufacturing of functionally graded material with SS 316L and IN625: microstructural and mechanical perspectives, CIRP Journal of Manufacturing Science and Technology 38 (2022) 230–242.
[42] ASTM A473-15, Standard Specification for Stainless Steel Forgings, W. C. ASTM International, PA., 2015.
[43] GB/T 3280-2015, Cold Rolled Stainless Steel Plate, sheet and strip -- CISA, 2015.
[44] Metals Handbook: Properties and Selection : Stainless Steels, Tool Materials and Special-Purpose Metals, Asm Intl, 1980.
[45] Y. Matsuoka, T. Iwasaki, N. Nakada, T. Tsuchiyama, S. Takaki, Effect of grain size on thermal and mechanical stability of austenite in metastable austenitic stainless steel, ISIJ Int. 53 (2013) 1224–1230.
[46] X.H. Chen, J. Lu, L. Lu, K. Lu, Tensile properties of a nanocrystalline 316L austenitic stainless steel, Scripta Mater. 52 (2005) 1039–1044.
[47] F. Yin, G.J. Cheng, R. Xu, K. Zhao, Q. Li, J. Jian, S. Hu, S. Sun, L. An, Q. Han, Ultrastrong nanocrystalline stainless steel and its Hall-Petch relationship in the nanoscale, Scripta Mater. 155 (2018) 26–31.
[48] A.N. Stroh, A theory of the fracture of, metals 6 (1957) 418–465.
[49] W.F. Zhu, N. Feng, Z.H. Chen, Y.K. Wang, S.Y. Zhang, Research on the Failure Form of Metal Parts, Technology Wind, 2019, p. 165.
[50] W. Qin, J. Li, Y. Liu, J. Kang, L. Zhu, D. Shu, P. Peng, D. She, D. Meng, Y. Li, Effects of grain size on tensile property and fracture morphology of 316L stainless steel, Mater. Lett. 254 (2019) 116–119.
[51] A. Das, S. Tarafder, Geometry of dimples and its correlation with mechanical properties in austenitic stainless steel, Scripta Mater. 59 (2008) 1014–1017.
[52] A. Das, S. Tarafder, Experimental investigation on martensitic transformation and fracture morphologies of austenitic stainless steel, Int. J. Plast. 25 (2009) 2222–2247.
[53] Q.P. Zhong, Z.H. Zhao, Z. Zhang, Development of fracture science and study on microscopic fracture mechanism, J. Mech. Strength (2005) 358–370.
[54] C. Du, J. Zhang, Y. Lian, X.M. Yuan, M.Y. Huo, Research status of residual stress in laser additive manufacturing, Surf. Technol. 48 (2019) 200–207.
[55] H.M. Wang, Laser additive manufacturing of high performance large metal components: some material base issues, Acta Aeronautica Astronautica Sinica 35 (2014) 2690–2698.
[56] R.L. Fan, Topology Optimization of Triple-strut Sunflower Cable Dome Nodes and Mechanical Properties of Additive Manufacturing Nodes, Master dissertation, Zhejiang University, 2021.
[57] S. Tukur, M. Dambatta, A. Ahmed, N. Mu'az, Effect of Heat Treatment Temperature on Mechanical Properties of the AISI 304 Stainless Steel,.
[58] D. Kong, C. Dong, X. Ni, L. Zhang, J. Yao, C. Man, X. Cheng, K. Xiao, X. Li, Mechanical properties and corrosion behavior of selective laser melted 316L stainless steel after different heat treatment processes, J. Mater. Sci. Technol. 35 (2019) 1499–1507.
[59] D. Kong, X. Ni, C. Dong, L. Zhang, C. Man, J. Yao, K. Xiao, X. Li, Heat treatment effect on the microstructure and corrosion behavior of 316L stainless steel fabricated by selective laser melting for proton exchange membrane fuel cells, Electrochim. Acta 276 (2018) 293–303.
[60] L. Yang, Effect of Solution Treatment on Microstructure and Properties of Wire Arc Printed 316L Stainless Steel, Thesis, Xi'an University of Technology, 2019.